Sánchez-González, Alberto; Santana, Domingo (2015). Solar flux distribution on central receivers: A projection method from analytic function, *Renewable Energy*, v. 74, pp.: 576-587.

Solar flux distribution on central receivers: a projection method from analytic function

Alberto Sánchez-González*, Domingo Santana

Universidad Carlos III de Madrid, Department of Thermal and Fluid Engineering, Av. de la Universidad, 30, 28911, Leganés, Madrid, Spain

*Corresponding author. Tel.: +34 916248884   E-mail address: asgonzal@ing.uc3m.es

Abstract

This paper presents a methodology to project the flux distribution from the image plane into the panels of any central receiver in Solar Power Tower plants. Since analytic functions derived from the convolution approach are conveniently defined on the image plane, its oblique projection solves the distorted spot found in actual receivers. Because of its accuracy describing the flux distribution due to rectangular focusing heliostats, we make use of the analytic function on the image plane by Collado et al. (1986). Based on the projection method, we have developed a computer code successfully confronted against PSA measurements and SolTrace software, either for flat plate or multi-panel cylindrical receivers. The validated model overcomes the computation time limitation associated to Monte Carlo technique, with a similar accuracy and even higher level of resolution. For each heliostat in a field, the spillage is computed besides the rest of optical losses; parallel projection is used for shading and blocking. The resulting optical performance tool generates the flux map caused by a whole field of heliostats. A multi-aiming strategy is investigated on the basis of the radius of the reflected beams, estimated from error cone angles.

Keywords: Solar power tower; Multi-panel cylindrical receiver; Flux density concentration; Oblique projection; Heliostat field optical efficiency; Multi-aiming strategy.

Nomenclature

AH	area of heliostat mirror [m^2]
ah, *aw*	limits of the convolution integral [m]
AR	area of receiver [m^2]
C	concentration ratio of flux density [-]
DNI	direct normal irradiance [W/m^2]
F	solar flux density [W/m^2]
f	optical loss factor [-]
G	origin of global coordinate system
H	center of heliostat mirror
k	aiming factor [-]
N	number [#]
n	normal unit vector
P_{inc}	Power incident on the receiver [W]
r	beam radius [m]
SLR	slant range [m]
s	unit vector pointing to the sun
T	target point
t	unit vector from *H* to *T*
THT	tower optical height [m]
u, **v**, **w**	unit vectors in *X*, *Y*, *Z*-direction
X, *Y*, *Z*	Cartesian coordinate axes
x, *y*, *z*	coordinates in *X*, *Y*, *Z*-direction [m]

Greek symbols

α	azimuth angle [rad]
Δx, Δy	nodal spacing in *X*, *Y*-direction [m]
ε	elevation angle [rad]
η	optical efficiency [-]
ξ, ζ	linear transformation of *x*, *y* [m]
ρ	reflectivity [-]
σ	error, standard deviation [mrad]
ω	incidence angle [rad]

Subscripts

at	atmospheric attenuation
e	effective
eq	receiver equator
h	heliostat
i, *j*	node index

int	interception
$k \cdot \sigma$	based on $k \cdot \sigma_e$
max	maximum, peak
mean	mean, averaged
p	panel of the receiver
pt	target panel
ref	reflected
sb	shading and blocking
sg	global system of coordinates
sh	heliostat system of coordinates
si	image plane system of coordinates
slp	mirror slope
st	target system of coordinates
sun	sunshape
trk	heliostat tracking

Superscripts

field	field of heliostats
hor	horizontal projection
image	projection into image plane
losses	optical losses
p	projection

1.   Introduction

In Central Receiver Systems (CRS), thousands of heliostats reflect solar radiation into the receiver. System design and optimization demand not only fast, but also accurate models to perform optical calculations. On the receiver surface, the distribution of flux density or its concentration ratio becomes the key outcome of these optical tools.

Existing models are divided into two categories [1]: Monte Carlo Ray Tracing (MCRT) and convolution methods. The first one is a statistical approach that traces a bundle of random rays from the sun. The more rays are traced the higher precision is achieved, but also higher computational cost, unaffordable for design and optimization studies. On the other hand, convolution methods rely on the mathematical superposition of error cones, namely: sunshape, concentration and mirror errors. While several approaches have been proposed to solve the convolution integral, all of them are faster than MCRT techniques.

Numerical resolution of the convolution integral with Fourier transform has been implemented in HELIOS code [2]. Such a resolution is highly accurate, but not fast enough for system design. Otherwise, the convolution integral can be solved analytically under certain assumptions, leading to an analytic expression for the flux density on the image plane, faster to evaluate. Lipps and Walzel [3] found an exact analytic result for flat (i.e. non-focusing) polygonal heliostats. Similarly, by means of analytic integration over a linearly mapped domain, Collado et al. [4] obtained an analytical expression based on the error function, which is suitable for rectangular focused heliostats. Such a model has been recently named UNIZAR [5].

Other authors have found approximate solutions for the flux density on the image plane. Assuming a Gaussian behavior for all error cones, a single circular normal distribution has been proposed [6]. Unlike other models, this simplified one can handle the astigmatism effect produced by off-axis aberration. The circular normal distribution has been implemented in HFLCAL code, which performs either optical or optimization simulations.

Walzel et al. [7] proposed a sixth order Hermite polynomial to represent the flux density on the image plane from flat heliostats. Its precision increases for small and distant heliostats. For focusing heliostats, a faceted heliostat composed of flat canted mirrors can be considered. Walzel's function has been implemented in DELSOL3 code [8], that takes a representative heliostat for each field sector, thus decreasing considerably computation time. In addition to optical performance calculations, DELSOL3 carries out optimization analysis scaling results from the performance run.

It has been detected a need for models to accurately predict the solar flux density on actual cylindrical receivers caused by an entire field of focusing heliostats. Since analytic functions are adequately defined on the image plane, we propose an oblique projection onto the receiver panels. This way, the

heliostat image shape is distorted appropriately. The analytic function on the image plane by UNIZAR has been adopted because of its accurate distribution of the solar flux density reflected by rectangular focusing heliostats.

A computer code has been developed based on the oblique projection methodology, which is described in the following section. Then, the model is first validated for flat plate receivers and secondly for cylindrical receivers, using experimental flux distributions and MCRT simulations. After validation of individual heliostats, the model is extended to an entire heliostat field, accounting for all the optical loss factors. At the end, flux maps are generated for several aiming strategies.

2.   Model based on projection

Analytic functions are usually defined on the plane normal to the central reflected ray and centered in the target point. This plane, named image plane, rarely coincides with any receiver plane. Therefore an appropriate transformation is claimed, namely oblique projection.

In this paper, we propose a methodology to project the solar flux density distribution from the image plane onto the receiver surfaces. The suggested procedure, summarized in Fig. 1, consists of four steps:

1. Receiver panels are discretized in a mesh of equally spaced nodes.

2. Mesh nodes are projected onto the image plane in the direction of the central reflected ray.

3. The analytic function is evaluated at the nodes on the image plane.

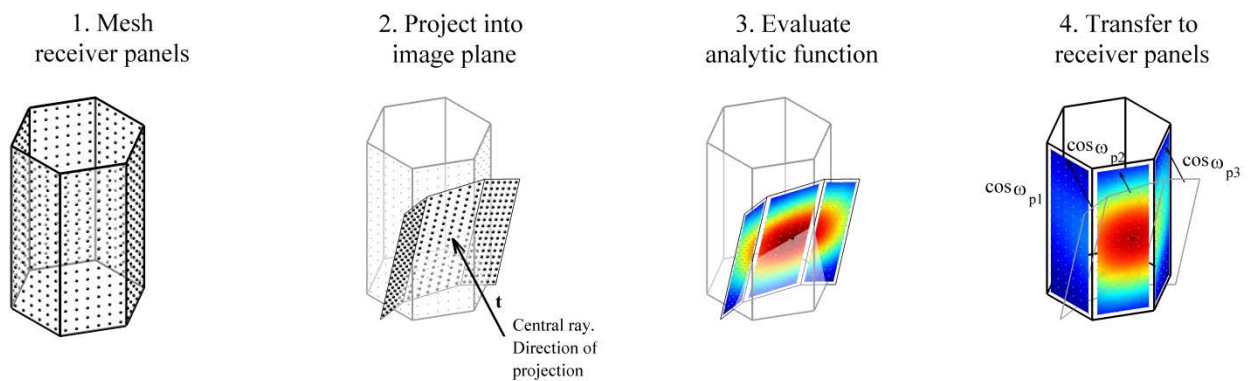4. Flux density at image nodes is multiplied by the cosine of the incidence angle on the receiver.

Fig. 1: Methodology of the model based on projection.

Since the ultimate goal is to project the flux distribution from the image plane to the receiver, an alternative procedure could be argued: first discretize the image plane and then project onto the receiver. Although the same goal is achieved, our proposed method offers several advantages. The discrete domain is strictly limited to the surfaces of interest, avoiding useless nodes. A unique mesh for the receiver also facilitates the sum of fluxes from the whole heliostat field.

The proposed model and, particularly, the projection step lead to three-dimensional geometric transformations, involving operations with vectors and matrices. A computer code has been developed, which deals with all types of central receivers made up of flat panels, either cylindrical or flat plate. Cylindrical receivers consist of any number of panels arranged in a cylindrical shell. Figures in this section correspond to a receiver of six panels. Obviously, the methodology herein described also applies to flat plate and cavity receivers.

A formulation based on the concentration ratio of flux density (*C*) is advantageous. This dimensionless parameter can be seen as the number of suns impinging on the receiver, regardless of the instantaneous solar insolation. Strictly speaking, the concentration of flux density is the ratio of flux density (*F*) on the receiver to the direct normal irradiance (*DNI*) incident on the heliostat field.

$$C = F/DNI \tag{1}$$

In this section, we describe in detail the four steps of the suggested procedure. Prior to that, we define various coordinate systems. The computation of spillage losses is presented at the end of this section.

2.1 Coordinate systems and transformations

The global system of coordinates (denoted as *sg*) has its origin *G* in the base of the tower at ground level. The positive X_{sg} axis points east and the positive Y_{sg} axis points north. As left handed coordinate system, the positive Z_{sg} axis is directed to the zenith.

Other Cartesian coordinate systems are locally placed. In each specific target point *T* on the receiver, a coordinate system (*st*) is defined. The $X_{st}Y_{st}$ plane is taken coplanar with the target panel, where the X_{st} axis is horizontal, the Y_{st} axis is vertical and the Z_{st} axis is outward normal to the panel. Also in *T*, a coordinate system referenced to the image plane (*si*) is set, as will be introduced in Section 2.3.

For each heliostat, a coordinate system (*sh*) is defined with origin in the mirror center *H*. The $X_{sh}Y_{sh}$ plane corresponds to the plane of the mirror and the Z_{sh} axis is outward normal to the mirror plane. For conventional rectangular heliostats with azimuth-elevation tracking, the Y_{sh} axis is parallel to the sides of the mirror and the X_{sh} axis remains horizontal as elevation axis.

Figure 2 illustrates the coordinate systems above mentioned. Throughout this paper, **u**, **v** and **w** stand for the unit vectors in the positive directions of *X*, *Y* and *Z* axes, respectively. Subscripts indicate the corresponding coordinate system.
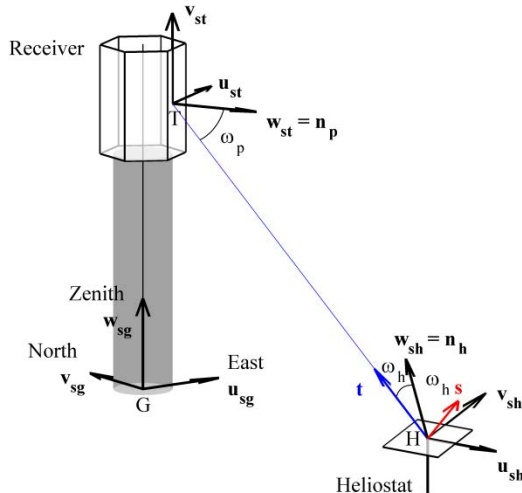
Fig. 2: Systems of coordinates.

The unit vector **s** points to the sun and is calculated with the correlation stated in [9] depending upon day and solar time. For a given heliostat with mirror center in H, **t** is the unit vector directed toward the aim point T. Thus, vector **t** is in the direction of the central reflected ray. According to Snell's law of reflection, the incident angle on the mirror equals the angle of reflection (ω_h). Then, the bisector of **s** and **t** is the heliostat normal (**n_h**), which coincides with **w_sh**.

$$\mathbf{n}_h = \frac{\mathbf{s}+\mathbf{t}}{|\mathbf{s}+\mathbf{t}|} = \mathbf{w}_{sh} \tag{2}$$

An appropriate transformation from the global system of coordinates (sg) to the heliostat coordinate system (sh) can be defined. Such a transformation comprises the translation from G to H and two consecutive rotations: azimuth and elevation. The heliostat azimuth angle (α_h) is zero for south orientation and positive in clockwise rotation, as shown in Fig. 3. The elevation angle (ε_h) is relative to the horizontal projection of the heliostat normal. Mathematically, the transformation from global to heliostat coordinates is expressed through the following matrix equation:

$$\begin{bmatrix} x \\ y \\ z \end{bmatrix}_{sh} = \begin{bmatrix} \cos\alpha_h & -\sin\alpha_h & 0 \\ \sin\alpha_h \cdot \sin\varepsilon_h & \cos\alpha_h \cdot \sin\varepsilon_h & \cos\varepsilon_h \\ -\sin\alpha_h \cdot \cos\varepsilon_h & -\cos\alpha_h \cdot \cos\varepsilon_h & \sin\varepsilon_h \end{bmatrix} \begin{bmatrix} x+H_x \\ y+H_y \\ z+H_z \end{bmatrix}_{sg} \tag{3}$$
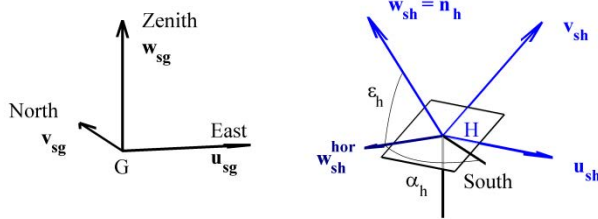

Fig. 3: Transformation from global to heliostat coordinate system.

External receivers are made of a number p of flat panels. A practical way of numbering the receiver panels is convenient. Fig. 4 shows the panels counterclockwise numbered starting from the south. The computer code allows any number of panels for the receiver, even single flat plate receiver.
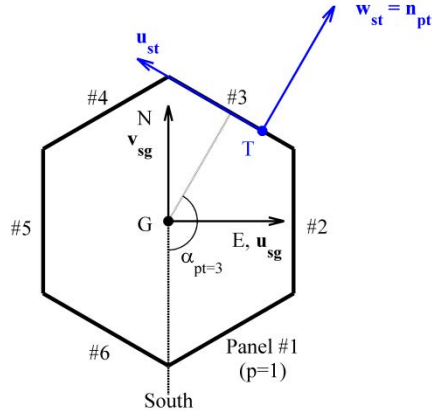
Fig. 4: Transformation from global to target coordinate system.

For a given aim point T, another transformation from global (sg) to local (st) system of coordinates can be defined. Such a transformation comprises the translation from G to T and a rotation of angle α_{pt}, which is the azimuth angle of the target panel. In matrix notation, this transformation is equivalent to the following equation:

$$\begin{bmatrix} x \\ y \\ z \end{bmatrix}_{st} = \begin{bmatrix} cos\,\alpha_{pt} & sin\,\alpha_{pt} & 0 \\ 0 & 0 & 1 \\ sin\,\alpha_{pt} & -cos\,\alpha_{pt} & 0 \end{bmatrix} \cdot \begin{bmatrix} x + T_x \\ y + T_y \\ z + T_z \end{bmatrix}_{sg} \tag{4}$$

Once the reference systems of coordinates have been established, the steps of the proposed model can be described in detail.

2.2 Receiver discretization

The first step of the suggested procedure (Fig. 1) is the discretization of the receiver surfaces, prior to its projection onto the image plane. Each receiver panel is discretized in a grid of nodes equally spaced. As schematically is illustrated in Fig. 5, the nodal spacing along horizontal and vertical directions is Δx and Δy, respectively. Because of geometric constrains, Δx and Δy cannot usually be exactly the same, although they approximate as much as possible ($\Delta x \approx \Delta y$). As usual, the finer the grid, the level of resolution increases, but also the computation time.

Since nodes placed in the edge of two panels would belong to both, such an indetermination has been avoided. In practice, each node in the mesh is located in the center of a cell whose area is equal to $\Delta x \cdot \Delta y$.
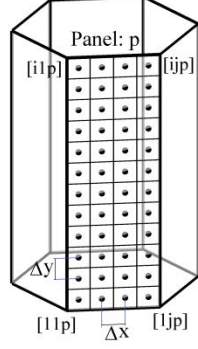
Fig. 5: Schematic discretization of a receiver panel.

Every single node can be identified by indices $[i,j,p]$. The last index (p) represents the number of panel, following the counterclockwise numbering previously introduced. Indices i and j stand for the row and column position, respectively. For convenience, $[i,j,p]$ indices start from the bottom left corner of each panel.

Following the order described above, a 3D matrix is created for any parameter of interest. Then, the value in each node is stored in its corresponding position in the matrix. When referring to the concentration of flux density (C) in a generic node, the following notation is used: $C_{i,j,p}$.

2.3 Mesh projection

The projection step is the core of the present model. The projection of the receiver mesh is performed from the receiver itself to the image plane, which is perpendicular to the central reflected ray with **t** unit vector. The projection is easily done referring the nodal coordinates to the image plane system.

The image system of coordinates (si), with origin in the target point T, matches the $X_{si}Y_{si}$ plane with the image plane. The X_{si} axis is kept horizontal, as X_{st} axis. In the direction of the Z_{si} axis, the $\mathbf{w_{si}}$ unit vector is equivalent to the opposite of vector **t**.

The transformation from target to image system of coordinates involves two rotations. The azimuth angle of rotation (α_t) is that of –**t** referred to the normal of the target panel. And the elevation angle of rotation (ε_t) is that of **t** relative to its horizontal projection. The positive rotation angles are displayed in Fig. 6, along with the target and the image systems of coordinates. In matrix notation, the transformation from target to image coordinate system is developed through the following equation:

$$
\begin{bmatrix} x \\ y \\ z \end{bmatrix}_{si} = \begin{bmatrix} \cos\alpha_t & 0 & \sin\alpha_t \\ -\sin\alpha_t \cdot \sin\varepsilon_t & \cos\varepsilon_t & \cos\alpha_t \cdot \sin\varepsilon_t \\ -\sin\alpha_t \cdot \cos\varepsilon_t & -\sin\varepsilon_t & \cos\alpha_t \cdot \cos\varepsilon_t \end{bmatrix} \cdot \begin{bmatrix} x \\ y \\ z \end{bmatrix}_{st}
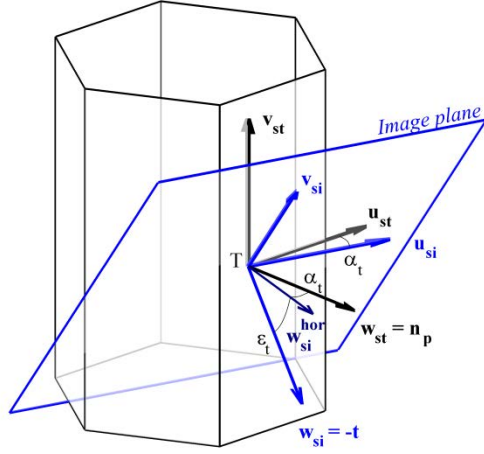\tag{5}
$$

10

Fig. 6: Transformation from target to image coordinate system.

Once in image coordinate system, the projection of the receiver nodes onto the image plane is straightforward. While x and y coordinates remains fixed, the z coordinate drops to zero, thus reaching the image plane. Symbolizing the projection onto the image plane with the superscript *image*, the projection is algebraically equivalent to:

$$
\begin{aligned}
x_{si}^{image} &= x_{si} \\
y_{si}^{image} &= y_{si} \\
z_{si}^{image} &= 0
\end{aligned}
\tag{6}
$$

At most, half of the receiver is visible from a heliostat position, while the other half is hidden. Hence, only the visible panels are projected onto the image plane.

The opposite direction of the central reflected beam, -**t**, has been assumed as the direction of projection. Actually, due to the divergence of sun rays there is not a sole reflected beam direction, even though the central ray represents the mean and most probable beam direction. The deviation increases with the distance from image plane to the receiving surface. Known the sunshape error, for a typical receiver with 4 m of radius, the maximum error is about one centimeter.

2.4 UNIZAR analytic function on the image plane

Collado et al. [4] defined two analytic functions for the solar flux density, both on the image plane and on the plane of flat plate receivers. Since linear mapping was assumed, the precision at receiver plane decreases when the angle of incidence with the panel (ω_p) increases. In other words, the image shape deformation found at the receiver is disregarded. Hence, the analytic function on the image plane has been adopted in the present study.

Hypothesis taken on UNIZAR model for the image plane represent adequately actual heliostats. The surface of rectangular heliostats is assumed to be continuous and spherical, being the focal length equal to the slant range (*SLR*). On-axis alignment is considered so that the astigmatic effect, experienced when the angle of incidence with the heliostat increases, is neglected.

UNIZAR expression for the solar flux density is based on the standard error function (erf). Following a matrix notation where *i* and *j* are nodal indices, the concentration ratio of flux density on the image plane becomes:

$$C_{i,j,p}^{image} = \frac{cos\,\omega_h}{4\cdot(1-cos\,\omega_h)^2}\Big[erf\big(\xi_{i,j,p}+aw\big)-erf\big(\xi_{i,j,p}-aw\big)\Big]\cdot\Big[erf\big(\zeta_{i,j,p}+ah\big)-erf\big(\zeta_{i,j,p}-ah\big)\Big] \quad (7)$$

The cosine of the incidence angle is the dot product of unitary vectors: $cos\,\omega_h = \mathbf{n}_h\cdot\mathbf{s} = \mathbf{n}_h\cdot\mathbf{t}$. The variables $\xi_{i,j,p}$ and $\zeta_{i,j,p}$ correspond to the linear transformation of x_{si} and y_{si} coordinates on the image plane, whereas *aw* and *ah* stand for the integration limits. These variables include in their definition the effective error (σ_e), which is the convolution of sunshape, mirror slope and heliostat tracking errors. Modeled these errors as circular Gaussian distributions whose standard deviations are σ_{sun}, σ_{slp} and σ_{trk}, respectively, their convolution σ_e is also a circular normal distribution with standard deviation:

$$\sigma_e = \sqrt{\sigma_{sun}^2 + 2(1+cos\,\omega_h)\sigma_{slp}^2 + \sigma_{trk}^2} \quad (8)$$

Hereafter sunshape standard deviation is 2.51 mrad, which was measured at the PSA. Further details about UNIZAR functions can be found in references [4,5].

2.5 Flux density on the receiver and spillage

The flux density in a node on the receiver is the same as that of its analogous node on the image plane, although affected by the angle of incidence with the receiver panel, ω_p. Therefore, the concentration ratio in node [*i,j*] belonging to panel *p* satisfies:

$$C_{i,j,p} = C_{i,j,p}^{image}\cdot cos\,\omega_p \quad (9)$$

Unfortunately, a portion of the flux reaching the image plane could not be intercepted by the receiver, incurring spillage losses. The intercept factor, f_{int}, is the fraction of solar flux reflected by the heliostat actually blocked by the receiver.

$$f_{int} = \frac{\bar{F}\cdot AR}{F_{ref}\cdot AH} \quad (10)$$

where $\overline{F}$ is the mean flux density on the receiver, AR is the area of the receiver, AH is the mirror area of the heliostat, and: $F_{ref}=DNI \cdot cos\omega_h$. The intercept factor is an outcome of the calculation of C. In terms of concentration of flux density in each node of the receiver, the above equation can be computed as:

$$f_{int} = \frac{\sum_{i,j,p} C_{i,j,p} \cdot \Delta x \cdot \Delta y}{cos\,\omega_h \cdot AH} \qquad (11)$$

where Δx and Δy are the horizontal and vertical spacing between nodes in the receiver. We can conclude that the intercept factor is a measure of not only the spillage, but also the loss due to the incidence angle on the receiver, implicit in the definition of C.

3.   Validation for flat plate receivers

The proposed model has been first validated for a flat plate receiver, which is the simplest case of external receiver. Our model has been confronted against experimental measurements from Plataforma Solar de Almería (PSA) and simulation results from SolTrace software, developed by the National Renewable Energy Laboratory [10].

The Monte Carlo Ray Tracing (MCRT) technique solves the solar energy collection and transmission according to the following procedure [11]: the Sun, considered as a massive source of sunlight, emits sunlight rays containing the same energy to ensure uniform distribution of sunlight; the sunlight transmission consists of four independent sub-processes (emission, reflection, transmission and absorption) following a specific probability distribution. In the present work, a bundle of 5 million random rays has been traced for each simulation.

During July 2004, experimental measurements were carried out around noon time in the CRS facility at PSA [12]. The images produced by individual heliostats on the flat plate receiver, at 35.16 m height, were captured. The Martin-Marietta at PSA is a 39.9 m^2 heliostat; 6.68 m width and 6.63 m height, but without mirror facets in a 0.66 m centered vertical strip. Three heliostat positions at PSA field have been selected for comparison, providing a wide variety of slant ranges and incidence angles on both the receiver panel (ω_p) and the heliostat (ω_h). For each heliostat position, its name and geometrical parameters are listed in Table 1. The slope errors have been taken from previous fitting, where the tracking error was neglected [5].

Table 1: Parameters of selected PSA heliostats.

Position name	SLR, m	$\cos \omega_p$	$\cos \omega_h$	σ_{slp}, mrad
C2	165.3	0.936	0.822	0.80
H61	100.0	0.716	0.895	1.40
H11	59.9	0.714	0.950	2.10

In the following three Figures, the normalized flux distribution on the receiver obtained with the proposed model is compared to that of the measured image (a) and to the SolTrace simulation output (b). Since the measured images provide levels of intensity, rather than flux density, the results in this section are expressed in normalized flux density, i.e. F/F_{max}. In each figure, the root mean square error (RMSE) between both contours is pointed out.
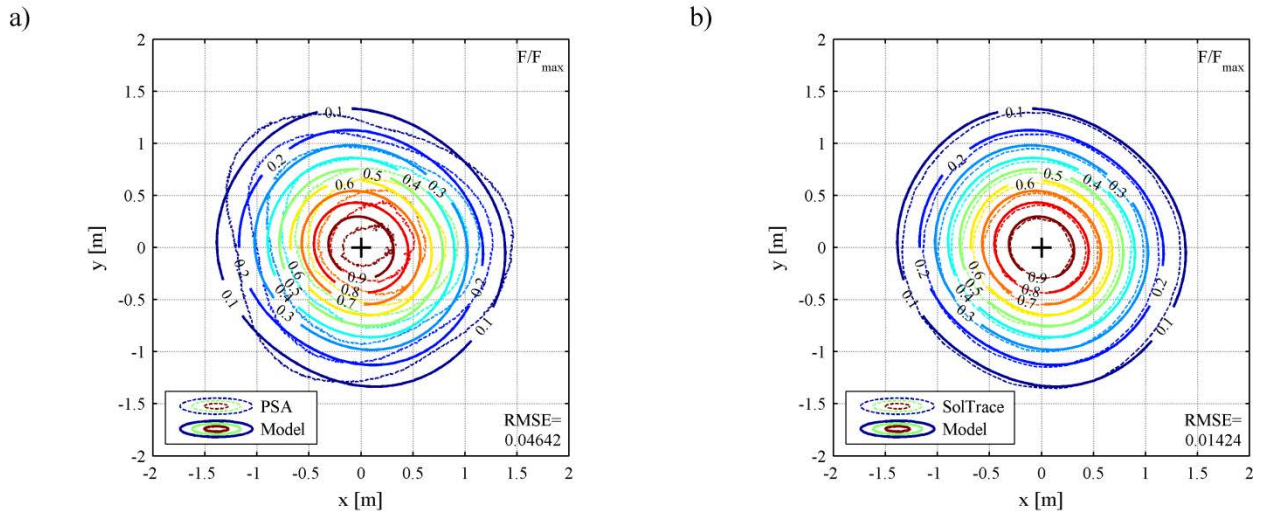
Fig. 7: Contours of normalized flux due to heliostat C2. Comparison of the model with: a) PSA measurement and b) SolTrace simulation.

The heliostat in position C2, Fig. 7, provides quasi-circular contours, where two symmetry axes can be envisaged. This shape is closely related to the standard error function used in the image plane. Since the solar reflected beam impacts nearly perpendicular to the receiver surface for this heliostat, such spot shape seems plausible.
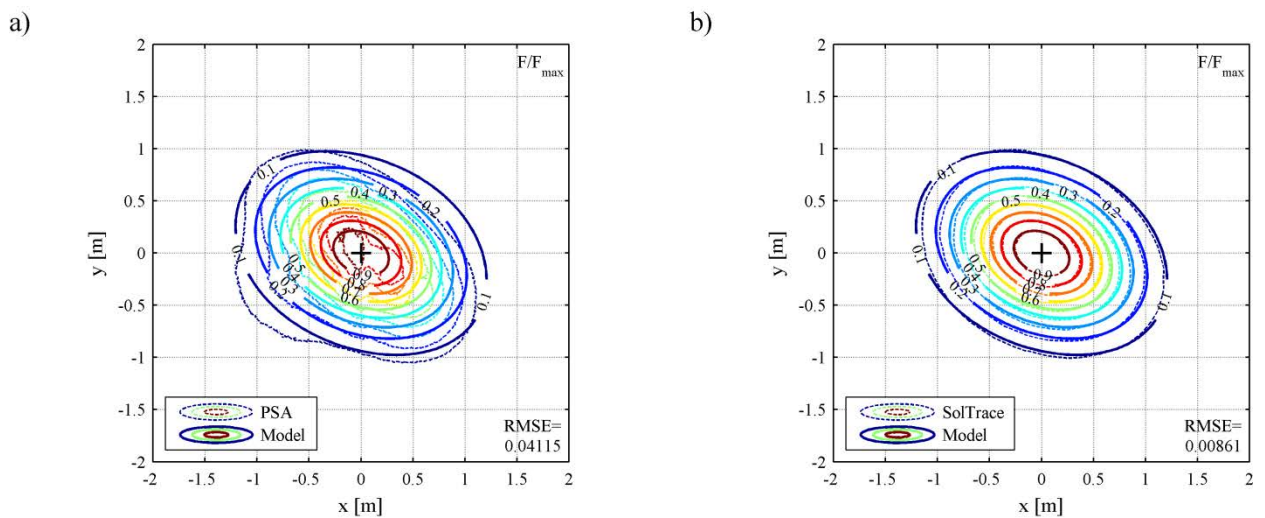

Fig. 8: Contours of normalized flux due to heliostat H61. Comparison of the model with: a) PSA measurement and b) SolTrace simulation.

While increasing the incidence angle on the receiver, ω_p, the distribution shape is stretched in the axis of the incident central ray, leading to quasi-elliptical contours, clearly evident in Fig. 8 and Fig. 9. For the positions in Table 1, the greater distortion is thus expected in heliostat H11.
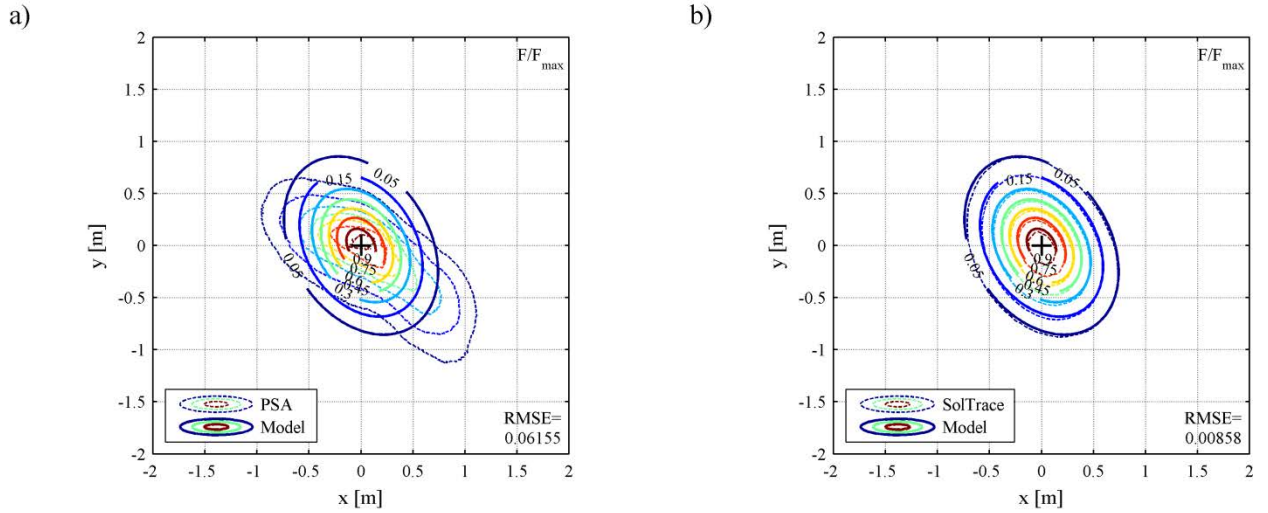
Fig. 9: Contours of normalized flux due to heliostat H11. Comparison of the model with: a) PSA measurement and b) SolTrace simulation.

Comparison between SolTrace and the suggested model shows excellent agreement. On-axis alignment has been considered in both codes, but the angle of incidence with the heliostat is a source of astigmatism [13]. Such aberration is not tackled in the model, whereas SolTrace simulates the real optical behavior. This methodological discrepancy can partially explain the 1.4% RMSE found in heliostat C2.

Compared to the experimental images, Figs. a), the general patterns are followed, while particular deviations can be encountered. The RMSE between both curves is around 4% in heliostats C2 and H61, and increases up to 6% in heliostat H11. For the latter (Fig. 9), differences are more evident. On the other hand, near the aim point where the flux densities are higher, experimental isolines are closer to the center than predicted by the model, as well as SolTrace.

Some disparities are associated with heliostat off-axis alignment, since heliostats were focused and canted for an aim point different to that during the experiments. Apart from heliostat alignment and experimental measurements uncertainty, other physical phenomena may explain spots measured. As an elastic structure, the heliostat frame deflects under wind and gravitational loads, affecting the beam optical quality [14]. Even temperature differences induce changes of curvature in the mirror facets, causing defocus [15].

Despite of acceptable experimental fluctuations, the proposed model can accurately predict the flux distribution on a flat plate receiver, independently of the incidence angle. For increasing incidence angles on the receiver, spot shapes are conveniently distorted likewise MCRT predictions.

4. Validation for multi-panel cylindrical receiver

The proposed model has been validated for the most general case: cylindrical receivers formed by any number of panels. The results herein presented correspond to a 16-panels cylindrical receiver. For selected heliostats in a surround field, the flux density distribution calculated with the suggested model is compared to SolTrace simulations.

A staggered heliostat field has been generated using the rules and parameters described in [16], assuming flat land. The field is composed of 3 zones with 35 heliostat in each row in the first zone. The densest heliostat field, not optimized, has been considered.

The rectangular heliostats are 12.305 m width and 9.752 m height, representing 120m² similarly to Gemasolar heliostats. For this kind of heliostat the errors of tracking, σ_{trk}, and slope, σ_{slp}, are 2.1 and 2.6 mrad, respectively [17]. The resulting field layout is shown in Fig. 10, where the resulting 4550 heliostats are distributed in 43 rows. First row radius is 87.46 m, and last one is 676.17 m.

The central receiver comprises 16 flat panels arranged around a cylindrical shell. For a cylinder of 8.5 m diameter, each panel width is 1.6908 m. The receiver, and each panel, is 10.5 m in height. The tower optical height (THT), vertical distance from the heliostat mirror center to the receiver equator, is set to 120 m.
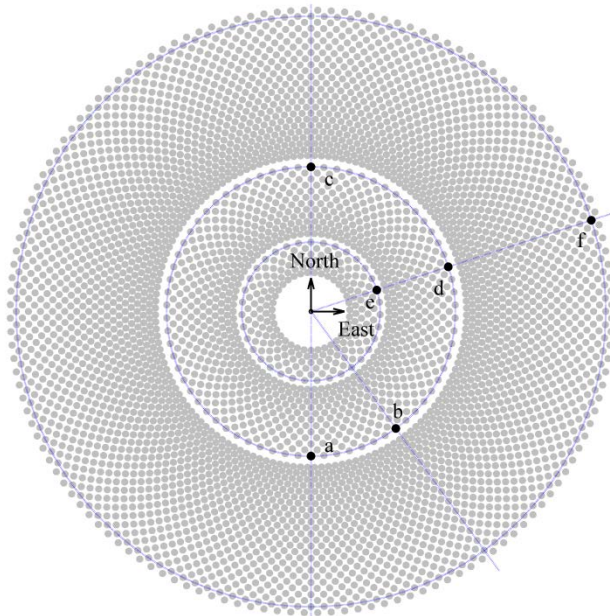

Fig. 10: Field layout and selected heliostats.

Noon time of Julian day number 81, i.e. equinox, has been considered in the results herein presented. For instance, the field is located at 37.1º latitude north, as PSA facility. Therefore, the solar altitude is 52.9º.

Six heliostat positions have been selected, black dots in Fig. 8. For a middle row, the azimuth position is varied in four heliostats (*a*, *b*, *c* and *d*); where heliostat *a* corresponds to sun position and heliostat *c* to anti-sun. Maintaining the azimuth of heliostat *d*, heliostats *e* and *f* are near and farther to the receiver, respectively. For the above mentioned instant of time, the cosine of the solar incidence angle on each heliostat is indicated in Table 3, together with location parameters.

Table 2: Location and incidence angle of selected heliostats.

Heliostat	Azimuth, deg	Row radius, m	*SLR*, m	$cos\ \omega_h$
a	0	324.49	341.91	0.598
b	-36	324.49	342.98	0.641
c	±180	324.49	341.91	0.96
d	-108	324.49	341.96	0.853
e	-108	155.45	193.01	0.906
f	-108	662.58	669.15	0.814

The distance between nodes in the receiver is 10 cm. This nodal spacing was selected from a compromise between CPU time and resolution. The gradient of concentration ratio between nodes is an indicator of such spatial resolution. For the near heliostat *e*, Fig. 11 illustrates the CPU time averaged over 10 realizations. For distances lower than 10 cm the computation time rapidly increases. On the other hand, the maximum gradient increases with the nodal spacing.
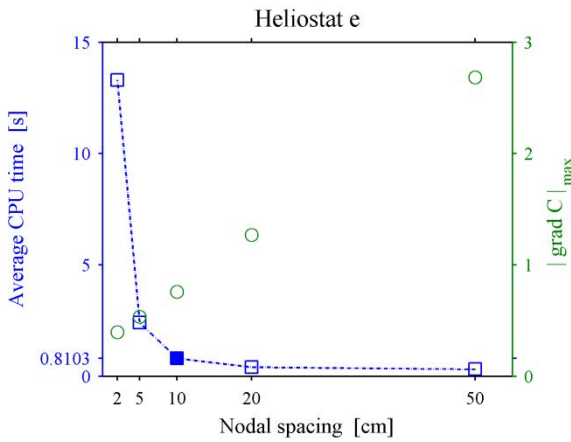

Fig. 11: CPU time and maximum gradient for different distance between nodes.

Simulations have been carried out in an Intel® Core™ i5-2400 microprocessor at 3.10 GHz with 4GB of RAM memory. Given 10 cm between nodes, our code takes 0.81 s on average. On the other hand, SolTrace simulations with 5 million rays, in the limit of that hardware, lasts an average time of 43.5 s, using a single core in both cases. The average CPU time employed by SolTrace using 0.5, 1, 2 and 5 millions of intercepted rays is represented in Fig. 12 for heliostat d at 342 m distance to the target point. Because it is a stochastic method, its accuracy and spatial resolution is dependent of amount of rays traced. Hence, the standard deviation of the power incident on the receiver, P_{inc}, based on 30 realizations is taken as a measure of the exactitude. Such dispersion decreases when the more rays are traced.
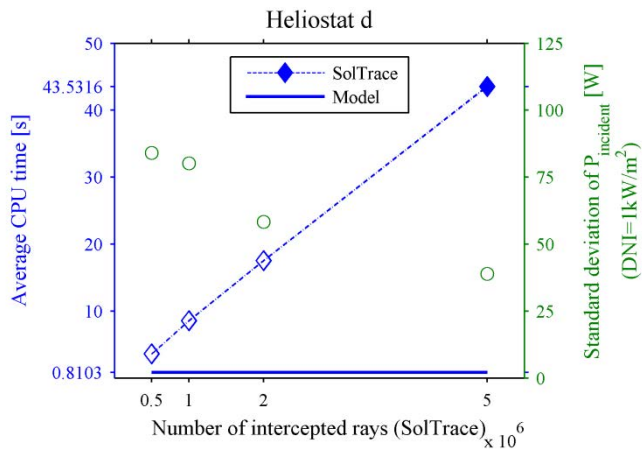

Fig. 12: CPU time and standard deviation of power incident on the receiver for different number of rays.

Computational cost can be argued to use convolution methods in design and optimization studies. However, modern CPU improvements and automatic MCRT parallelization, currently implemented in SolTrace, is closing the gap between both techniques.

The flux distribution from each selected heliostat is below showed. Results are expressed in terms of the concentration ratio of flux density, as defined in Eq. (1). Therefore, data are independent of instantaneous solar radiation. Since Eq. (9) is used, loss factors because of reflectivity, attenuation and shading and blocking have been neglected.

For each individual heliostat, Fig. 13 shows the contours of flux density concentration on the unfolded surface of the receiver. Only the corresponding half visible side of the receiver is represented; each panel number is displayed at the top. Solid lines correspond to the present model, while dashed lines correspond to SolTrace simulation.
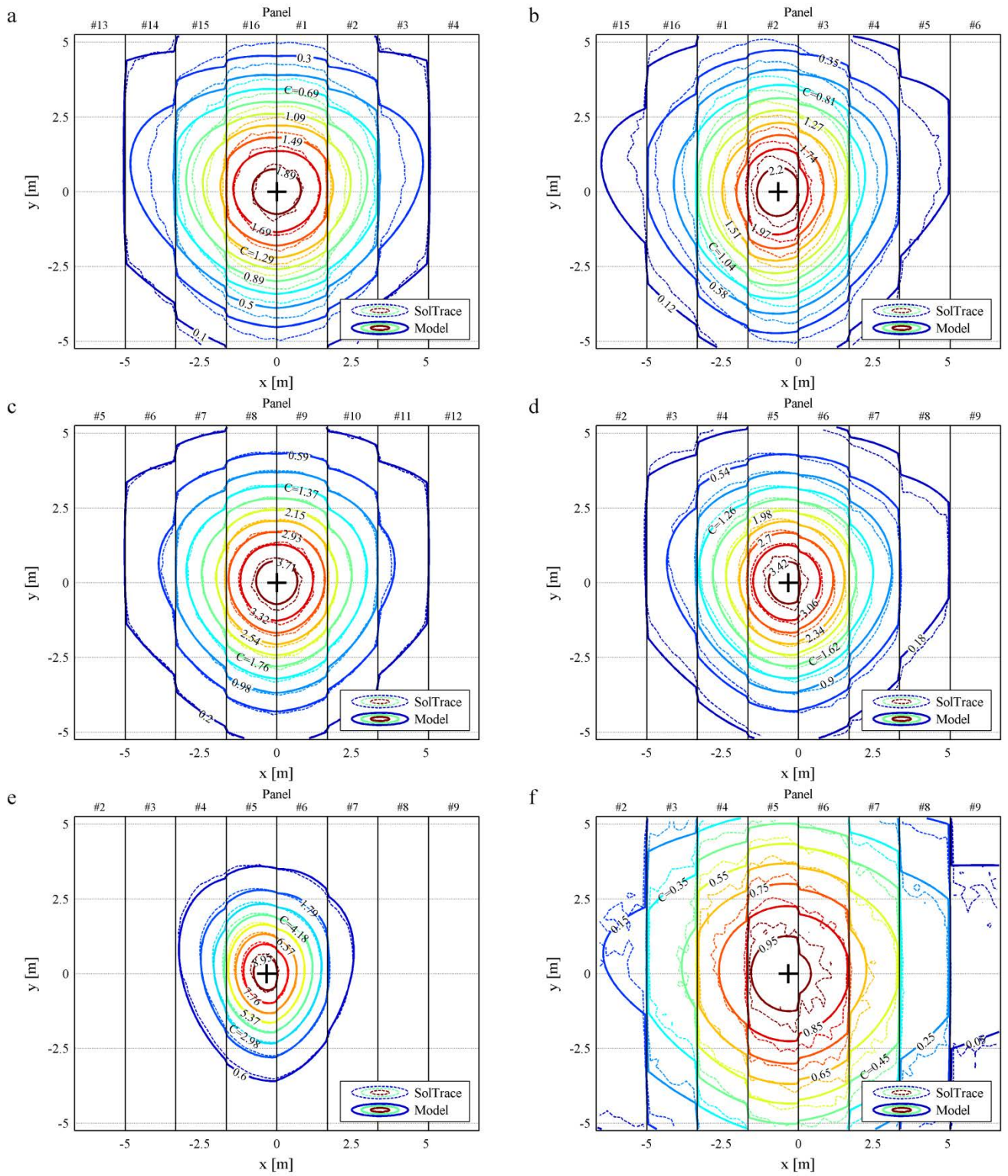
Fig. 13: Contours of concentration ratio of flux density for heliostats *a*, *b*, *c*, *d*, *e* and *f*.

For the anti-sun position, heliostat *c*, contours lines by the model fit well the SolTrace simulation. Isolines seem to slightly separate when the heliostat cosine decreases. Even for the worst case, heliostat *a*, differences are not significant. Astigmatic aberrations, solved by SolTrace, are again the error source.

Despite the differences commented in the paragraph above, the proposed model follows the shapes simulated with SolTrace. For the same row, the heliostats in the position of sun (*a*) and anti-sun (*c*) produce similar image shapes, while the former is wider. Heliostats in intermediate positions (*b* and *d*) lead to image sizes between those, and rotated at the same time.

For a given azimuth angle, the heliostat image is smaller the closer the heliostat is to the receiver (*e*). Differences between the model and MCRT simulation emerge when the slant range increases. As beam diameter at the focus broadens, 5 million rays do not provide enough resolution, which explains the ripples found in SolTrace isolines for heliostat *f*. In the side panels where the incidence angle is larger, image shapes are distorted as anticipated for flat plate receivers.

The intercept factor calculated with Eq. (11) has been compared to SolTrace output (Table 3). For the selected heliostats, this factor is underestimated by the model, even though deviations do not reach 2%. Insignificant underestimation is also found in the average and peak concentration ratios, listed in Table3.

Table 3: Intercept factor, mean and peak concentration ratio for the model and SolTrace.

Heliostat	f_{int}		C_{mean}		C_{max}	
	Model	SolTrace	Model	SolTrace	Model	SolTrace
a	0.917	0.933	0.463	0.472	1.985	2.028
b	0.928	0.939	0.503	0.509	2.318	2.440
c	0.945	0.953	0.767	0.773	3.910	4.040
d	0.948	0.955	0.683	0.688	3.597	3.685
e	1	1	0.765	0.766	9.551	9.844
f	0.596	0.608	0.410	0.419	0.998	1.046

To sum up, the proposed model replicates the distributions simulated with SolTrace, using 50 times less computation time. Furthermore, the spatial resolution can be greater than that of the MCRT simulation.

5.   Flux map by a field of heliostats

Once the model is validated for individual heliostats, the code has been extended to integrate the flux density distributions caused by the whole field.

5.1 Concentration ratio and optical efficiency

The concentration ratio of flux density defined in Eq. (9) does not take into account the optical losses, except for cosine effects and spillage, which are implicitly included. All other loss factors affecting the flux density are: mirror reflectivity, ρ, atmospheric attenuation, f_{at}, and shading and blocking, f_{sb}. Then, the concentration ratio in receiver node $[i,j,p]$ due to a single heliostat accounting for all losses is:

$$C_{i,j,p}^{losses} = \rho \cdot f_{sb} \cdot f_{at} \cdot C_{i,j,p} \tag{12}$$

The heliostat optical efficiency is the product of the loss factors: $\eta_h = \cos \omega_h \cdot \rho \cdot f_{sb} \cdot f_{at} \cdot f_{int}$. The reflectivity, ρ, is a property of the mirror and also depends on its cleanliness. Hereafter this factor has been neglected ($\rho=1$). The attenuation factor, f_{at}, is primarily influenced by the heliostat distance to the target point, i.e. the slant range. One of the simplest correlation is [18]:

$$f_{at} = 0.99321 - 0.000176 \cdot SLR + 1.97 \cdot 10^{-8} \cdot SLR^2 \tag{13}$$

The shading and blocking factor, f_{sb}, is defined as the fraction of heliostat mirror that is neither shadowed nor blocked by neighbor heliostats. Due to its quick computation, parallelism between neighbor heliostat planes is assumed [19]. Shading potential is initially assigned to 14 neighbor heliostats, 3 of which may also block. However, those neighbors behind the plane of the heliostat are finally ignored, halving the number of neighbors projected. The shadowed/blocked mirror area is found in the intersection between the boundaries of the heliostat and those projected from its neighbors. To facilitate the computation, the coordinate system is transformed from global to heliostat, following Eq. (3). The calculation of shadowing and blocking factor has been successfully compared with the results published in [16].

To obtain the concentration ratio from a whole heliostat field, the concentration by each heliostat obtained from Eq. (12) is summed in every single node on the receiver mesh.

$$C_{i,j,p}^{field} = \sum_{heliostats} C_{i,j,p}^{losses} \tag{14}$$

The optical efficiency of a field consisting of N_h heliostats is equal to the averaged heliostat efficiency: $\eta_{field} = \sum_{heliostats} \eta_h \bigg/ N_h$. This is the figure of merit usually utilized in optimization studies [20].

5.2 Flux map on the receiver

From the field of 4550 heliostats introduced in the preceding section (Fig. 10), the overall distribution of flux density on the receiver has been computed by means of Eq. (14). The simulation takes around 1 hour in all, while SolTrace would last around 50 hours (12.5 hours using 4 cores). All heliostats are aimed at the receiver equator (THT=120 m), which is the simplest aiming strategy. On a 3D view of the receiver, Fig. 14a represents the contours of concentration ratio of flux density for the equinox at noon time. Such flux map is also drawn in a 2D plot on the unfolded surface of the 16-panels cylindrical receiver (b).
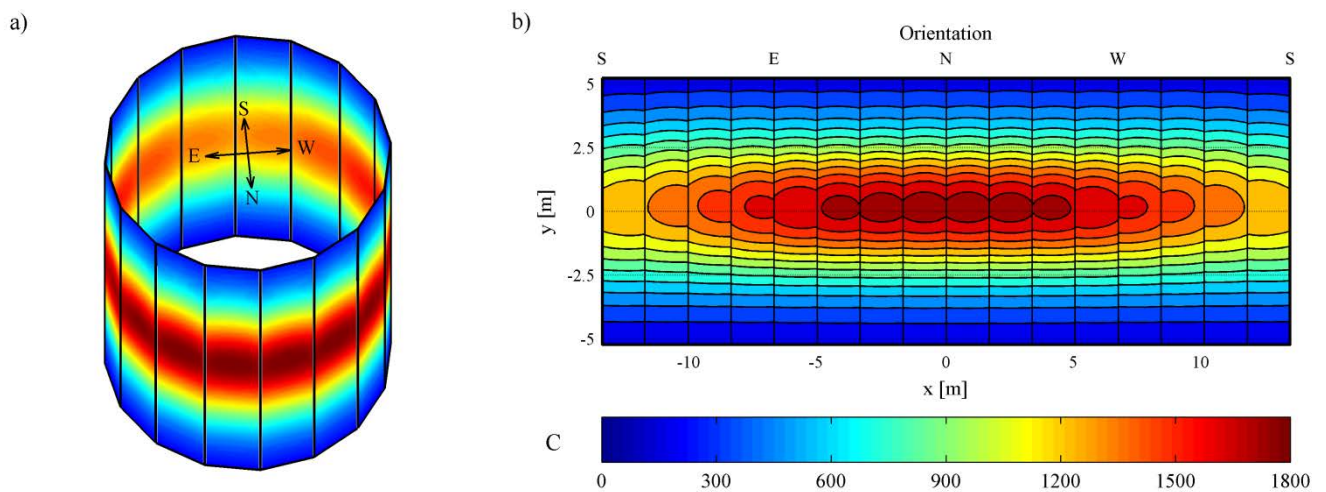

Fig. 14: Concentration ratio of flux density at equinox noon for single aiming. a) 3D view and b) unfolded 2D view.

Symmetry about the north direction was expected at noon. The mean flux concentration is equal to 895, which represents the flux density of 895 suns at that instant of time; while the peak concentration is 1806. For any x-coordinate, the maximum concentration value is found slightly above the receiver equator. Although all heliostats are aimed at y=0, this is because adjacent panels are reached on average somewhat above. This effect is also revealed for individual heliostats in Fig. 13. The intercept factor is equal to 0.804 with equatorial aiming, which represents the upper limit for this heliostat field. These parameters and the overall optical efficiency are reported in Table 5.

An animated video is included illustrating the heliostat field and the flux concentrations on the receiver throughout the equinox daytime. Shadowed and blocked mirror areas are there represented in black and cyan, respectively. Since the field is the densest possible many blocking and shading losses occur, particularly near sunrise and sunset. Even at noon, the overall shading and blocking factor is as low as 0.798.

Video 1 [around here]: Animation of heliostat field and flux concentration on the receiver throughout Equinox daytime with single aiming.

6.   Multi-aiming strategy

Non-uniform flux distributions induce high thermal stress on receiver tubes, which is a critical factor in receiver design and operation [21,22]. In contrast to single aim, multi-aiming strategies can flatten the flux distribution on the receiver to reduce thermal stresses and enhance the receiver efficiency. A multi-aiming strategy entails adjusting each heliostat target position along the vertical direction on the surface of the cylindrical receiver. The position of the aim point can be estimated from the radius of the reflected beam, as suggested by Vant-Hull [23]. Then, the heliostat is aimed at the receiver in such a way that the beam circumference is tangent to either the upper or the lower receiver edge.

The reflected sunshape and its associated errors have been modeled in Eq. (8) as circular Gaussian distributions convolved into the effective error σ_e. For a normal distribution, 68% of the reflected flux is within the beam subtended under σ_e, 95% under $2\sigma_e$ and 99.7% under $3\sigma_e$. The beam radius ($r_{k\sigma}$) depends directly on the adopted error angle, $k \cdot \sigma_e$, where k is defined as an aiming factor that typically ranges between 0 and 3. Since $k \cdot \sigma_e$ is small, the radius of the reflected beam at the image plane can be estimated as:

$$r_{k\sigma} = SLR \cdot k \cdot \sigma_e \qquad (15)$$

The target point $T_{k\sigma}$ is located from the upper or the lower edge, in alternate heliostat rows, at a distance equal to the projection of the beam radius ($r_{k\sigma}^p$). For cylindrical receivers, the beam radius projection into the receiver vertical satisfies:

$$r_{k\sigma}^p = \frac{r_{k\sigma}}{\cos \varepsilon_t} = \frac{SLR \cdot k \cdot \sigma_e}{\cos \varepsilon_t} \qquad (16)$$

where ε_t is the elevation angle of the **t** target vector, as previously stated. If the projection of the beam diameter is greater than the receiver height, then the heliostat is aimed at the receiver equator, T_{eq}. Fig. 15 illustrates the above described multi-targeting process, which comprises: (a) estimation of the beam radius and its projection based on preliminary equatorial aiming, and (b) positioning of the aim point. Since heliostats are aligned for a fixed target point, usually the equator, small –negligible– astigmatic aberrations are presumed for displaced aiming.
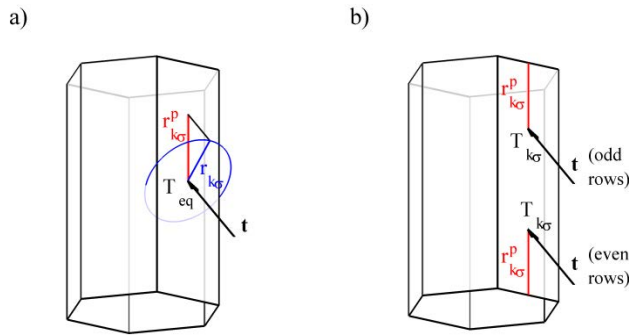
Fig. 15: Multi-aiming process: a) estimation of beam radius, and b) target positioning.

Flux maps on the receiver have been again calculated at equinox noon using the multi-aiming strategy. For beam radii based on error angles $3\sigma_e$, $2\sigma_e$ and σ_e, Fig. 16 represents the distributions of concentration ratio of flux density, where contour levels are kept the same as in Fig. 14. When $k=3$ (Fig. 16a), the flux pattern is similar to that with equatorial aiming, as expected. However, the peak concentration ratio is reduced to 1770 by slightly broadening the hot spot, while the mean concentration ratio and the intercept factor remain almost equal to those with single aiming (Table 4).
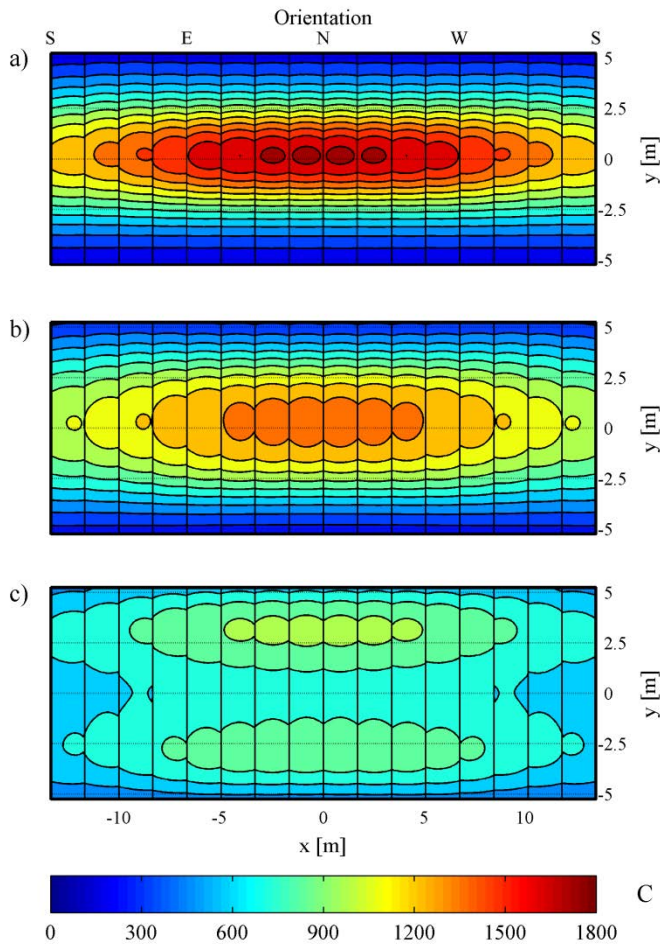
Fig. 16: Concentration ratio of flux density at equinox noon for multi-aiming based on: a) $3\sigma_e$, b) $2\sigma_e$ and c) σ_e.

An aiming strategy based on $2\sigma_e$ substantially flattens the flux distribution along the equator belt (Fig. 16b). At equinox noon, this aiming has the advantage of a more uniform distribution while the flux intercepted by the receiver is basically the same as for the above mentioned strategies. Now, the peak flux ratio falls to 1421. The latter and other parameters are reported in Table 4 for all the cases.

Table 4: Optical efficiencies and concentration ratios.

Aiming		f_{int}	η_{field}	C_{max}	C_{mean}
Single	equatorial	0.804	0.466	1806	895.0
	$3\cdot\sigma_e$	0.804	0.465	1770	894.6
Multiple	$2\cdot\sigma_e$	0.796	0.460	1421	883.5
	$1\cdot\sigma_e$	0.707	0.405	1007	778.7

Lastly, a multi-aiming strategy based on $k=1$ generates a different flux pattern (Fig. 16c), where two hot strips are found above and below the equator. The softer spot at the bottom is mainly attributed to greater blocking losses as the height of the aim point diminishes. Compared to the other cases, spillage increases significantly (Table 4).

7.   Conclusions

We have presented a 4-step methodology to determine the flux density distribution on central receivers of flat panels. This procedure relies on the oblique projection onto the receiver from the flux distribution on the image plane. This is accomplished by a simple coordinate system transformation, implemented in a computer code.

In this paper, the projection method has been applied on the basis of the analytic function at the image plane by Collado et al. [4]. The resulting model solves the distorted spot found when the incidence angle on the receiver increases. For any given rectangular focusing heliostat, the model compares successfully to both PSA measurements and SolTrace simulations. Compared to the latter, our code underestimates up to 2% the receiver interception. Considerable computation time is saved over MCRT, all of this with similar degree of accuracy and even higher resolution level for far heliostats.

The developed tool generates the flux maps caused by an entire field of heliostats, considering shading and blocking in addition to the rest of optical losses. The distributions of flux density on the surface of central receivers are modified through a multi-aiming strategy based on the radius of each heliostat beam. For the staggered heliostat field in this paper, a rather uniform distribution is obtained when the beam radius is estimated from an error angle equal to $2\sigma_e$.

This optical performance tool can be applied to the investigation of the interaction between the heliostat field and the thermal receiver. Also optimization analyses can be conducted, taking advantage of its accuracy and computation speed.

Acknowledgments

References

[1] Garcia P, Ferriere A, Bezian J-J. Codes for solar flux calculation dedicated to central receiver system applications: A comparative review. Sol Energy 2008;82:189–97.

[2] Biggs F, Vittitoe CN. Helios model for the optical behavior of reflecting solar concentrators. Sandia National Laboratories, Albuquerque, New Mexico: SAND-76-0347; 1979.

[3] Lipps FW, Walzel MD. An analytic evaluation of the flux density due to sunlight reflected from a flat mirror having a polygonal boundary. Sol Energy 1978;21:113–21.

[4] Collado FJ, Gómez A, Turégano JA. An analytic function for the flux density due to sunlight reflected from a heliostat. Sol Energy 1986;37:215–34.

[5] Collado FJ. One-point fitting of the flux density produced by a heliostat. Sol Energy 2010;84:673–84.

[6] Schwarzbözl P, Schmitz M, Pitz-paal R. Visual HFLCAL - A software tool for layout and optimisation of heliostat fields. SolarPACES, Berlin, Germany: 2009.

[7] Walzel MD, Lipps FW, Vant-Hull LL. A solar flux density calculation for a solar tower concentrator using a two-dimensional Hermite function expansion. Sol Energy 1977;19:239–53.

[8] Kistler BL. A user's manual for DELSOL3: Computer code for calculating the optical performance and optimal system design for solar thermal central receiver plants. Sandia National Laboratories, Livermore, California: SAND-86-8018; 1986.

[9] Duffie JA, Beckman WA. Solar engineering of thermal processes. New York: Wiley; 1991.

[10] Wendelin T, Dobos A, Lewandowski A. SolTrace: A Ray-Tracing Code for Complex Solar Optical Systems. vol. 303. National Renewable Energy Laboratory, Golden, Colorado: NREL/TP-5500-59163; 2013.

[11] Wang F, Shuai Y, Tan H, Zhang X, Mao Q. Heat transfer analyses of porous media receiver with multi-dish collector by coupling MCRT and FVM method. Sol Energy 2013;93:158–68.

[12] Monterreal R. Personal communication 2013.

[13] Igel EA, Hughes RL. Optical analysis of solar facility heliostats. Sol Energy 1979;22:283–95.

[14] Strachan JW, Houser RM. Testing and evaluation of large-area heliostats for solar thermal applications. Sandia National Laboratories, Albuquerque, New Mexico: SAND92-1381; 1993.

[15] Jones SA, Edgar RM, Houser RM. Recent results on the optical performance of solar two heliostats. 1994.

[16] Collado FJ, Guallar J. Campo: Generation of regular heliostat fields. Renew Energy 2012;46:49–59.

[17] Augsburger G, Favrat D. Modelling of the receiver transient flux distribution due to cloud passages on a solar tower thermal power plant. Sol Energy 2013;87:42–52.

[18]   Leary PL, Hankins JD. User's guide for MIRVAL: a computer code for comparing designs of heliostat-receiver optics for central receiver solar power plants. Sandia National Laboratories, Livermore, California: SAND-77-8280; 1979.

[19]   Collado FJ, Guallar J. Design of solar tower plants heliostat by heliostat: The blocking factor. SolarPACES, Berlin, Germany: 2009.

[20]   Besarati SM, Yogi Goswami D. A computationally efficient method for the design of the heliostat field for solar power tower plant. Renew Energy 2014;69:226–32.

[21]   Boerema N, Morrison G, Taylor R, Rosengarten G. High temperature solar thermal central-receiver billboard design. Sol Energy 2013;97:356–68.

[22]   Rodríguez-Sánchez M, Soria-Verdugo A, Almendros-Ibáñez JA, Acosta-Iborra A, Santana D. Thermal design guidelines of solar power towers. Appl Therm Eng 2014;63:428–38.

[23]   Vant-Hull LL. The Role of "Allowable Flux Density" in the Design and Operation of Molten-Salt Solar Central Receivers. J Sol Energy Eng 2002;124:165.